



# Dynamics of a Blended Lithium-Ion Battery Electrode During Galvanostatic Intermittent Titration Technique



Z. Mao, M. Farkhondeh, M. Pritzker, M. Fowler\*, Z. Chen

Department of Chemical Engineering, University of Waterloo, 200 University Avenue West, Waterloo, Ontario N2L 3G1, Canada

## ARTICLE INFO

### Article history:

Received 20 April 2016

Accepted 29 November 2016

Available online 29 November 2016

### Keywords:

model

lithium-ion battery

blended cathode

GITT

NMC

LMO

## ABSTRACT

A multi-particle model is developed and applied to the data from galvanostatic intermittent titration technique (GITT) experiments with varying pulse currents and relaxation periods on a  $\text{LiNi}_{1/3}\text{Mn}_{1/3}\text{Co}_{1/3}\text{O}_2 - \text{LiMn}_2\text{O}_4$  (NMC-LMO) blended lithium-ion electrode. The good agreement between the simulated and experimental potential-time curves shows that the model is applicable for all GITT conditions considered, but more accurate for the case of small current pulse discharges with long relaxation times. Analysis of the current contribution and the solid-state surface concentration of each active component in the blended electrode shows a dynamic lithiation/delithiation interaction between the two components and between micron and submicron NMC particles during the relaxation periods in the GITT experiments. The interaction is attributed to the difference in the equilibrium potentials of the two components at any given stoichiometry which redistributes the lithium among LMO and NMC particles until a common equilibrium potential is reached.

© 2016 Elsevier Ltd. All rights reserved.

## 1. Introduction

Blended cathodes have been adopted within the growing electric vehicle market to further improve the electrode performance of lithium-ion batteries (LIB) for hybrid-electric vehicles (HEVs) and plug-in hybrid-electric vehicles (PHEVs) [1]. The blending of different crystalline structure materials such as layered-spinel mixtures ( $\text{LiNi}_x\text{Co}_y\text{Al}_{1-x-y}\text{O}_2 - \text{LiMn}_2\text{O}_4$  (NCA-LMO) [2,3],  $\text{LiNi}_x\text{Mn}_y\text{Co}_{1-x-y}\text{O}_2 - \text{LiMn}_2\text{O}_4$  (NMC-LMO) [4]), layered-layered mixtures ( $\text{LiNi}_x\text{Co}_y\text{Al}_{1-x-y}\text{O}_2 - \text{LiCoO}_2$  (NCA-LCO) [5]), layered-olivine mixtures ( $\text{LiCoO}_2 - \text{LiFePO}_4$  (LCO-LFP) [6]), spinel-olivine mixtures ( $\text{LiMn}_2\text{O}_4 - \text{LiFePO}_4$  (LMO-LFP) [7]) allows the best properties of the individual active materials to be combined to improve the energy or power density as well as the cycling and storage durability. If successful, the electrochemical performance of blended cathodes would be expected to be superior to that of single material systems.

NMC-LMO blended systems for electric vehicle applications have been recently developed by several battery companies [1,4]. Cathodes made of spinel LMO have a high operating potential and good rate capability while NMC cathodes have high capacity and good capacity retention. Therefore, a mixture of NMC and LMO

yields an electrode with a balanced electrochemical performance in terms of specific capacity and working potential. However, LMO is plagued with fast capacity fade (poor cycle life) and low capacity retention after long-term storage at elevated temperatures. This behavior is mainly attributed to Mn dissolution and its subsequent reduction at the anode (e.g., graphite in a full LMO/graphite cell) [8,9], which causes the interfacial contact resistance [8] and charge-transfer impedance at the interface between graphite and electrolyte [10] to rise and a coulombic imbalance to develop [11]. Fortunately, when LMO is mixed with NMC as a blended cathode, a synergistic interplay between the two materials is observed. The presence of NMC appears to suppress Mn dissolution and enable the blended cathode to exhibit cycling or storage performance that is often better than expected from a LMO electrode [11–13].

The galvanostatic intermittent titration technique (GITT) is a very powerful electrochemical procedure that has been used to analyze the dynamics of electrode processes such as material phase formation, structural transitions or mass transport and estimate the corresponding parameters. A number of researchers have applied this method to study lithium-ion batteries. For example, Dees et al. [14] and Gowda et al. [15] investigated the polarization and relaxation behavior of lithium- and manganese-rich layered transition metal oxides to understand the structural transitions that occur in the cathode. Gallagher et al. [16] used GITT to evaluate the rate constants for phase formation and consumption of lithiated graphite. Bach et al. [17] carried out GITT

\* Corresponding author. Tel.: +1 519 888 4567, ext 33415, fax: +1 519 888 4347  
E-mail address: [mfowler@uwaterloo.ca](mailto:mfowler@uwaterloo.ca) (M. Fowler).

## Nomenclature

$A$	cathode area ( $\text{cm}^2$ )
$a_{n,m}$	specific surface area of active material $n$ with particle size class $m$ ( $\text{m}^{-1}$ )
$c_{n,m}$	Li ion concentration in active material $n$ with particle size class $m$ ( $\text{mol m}^{-3}$ )
$c_e$	Li ion concentration in electrolyte ( $\text{mol m}^{-3}$ )
$c_T$	total Li ion concentration in electrolyte ( $\text{mol m}^{-3}$ )
$c_n^{\text{max}}$	maximum concentration of Li within active material $n$ ( $\text{mol m}^{-3}$ )
$D_n$	solid-phase binary diffusion coefficient in active material $n$ ( $\text{m}^2 \text{s}^{-1}$ )
$D_e$	diffusion coefficient of electrolyte based on a thermodynamic driving force ( $\text{m}^2 \text{s}^{-1}$ )
$D_{n,m}$	Li ion solid-phase diffusion coefficient in active material $n$ with particle size class $m$ ( $\text{m}^2 \text{s}^{-1}$ )
$D_{\text{eff,sep}}$	effective diffusion coefficient of electrolyte in separator ( $\text{m}^2 \text{s}^{-1}$ )
$D_{\text{eff,cat}}$	effective diffusion coefficient of electrolyte in cathode ( $\text{m}^2 \text{s}^{-1}$ )
$D_e$	bulk diffusion coefficient in the electrolyte ( $\text{m}^2 \text{s}^{-1}$ )
$E$	cell potential (V)
$F$	Faraday constant ( $96480 \text{C mol}^{-1}$ )
$f_{\pm}$	mean molar activity coefficient of inorganic salt in electrolyte
$I$	applied current (A)
$i_{n,m}^0$	exchange current density for lithiation/delithiation on active material $n$ with particle size class $m$ ( $\text{A m}^{-2}$ )
$i_1$	solid-phase current density ( $\text{A m}^{-2}$ )
$i_2$	liquid-phase current density ( $\text{A m}^{-2}$ )
$i_{n,m}$	faradaic current density on active material $n$ with particle size class $m$ ( $\text{A m}^{-2}$ )
$i_f^0$	exchange current density for charge transfer reaction on Li foil ( $\text{A m}^{-2}$ )
$k_n$	rate constant ( $\text{mol m}^{-2} \text{s}^{-1} (\text{mol m}^{-3})^{-3/2}$ )
$L$	electrode thickness (m)
$L_{\text{sep}}$	separator thickness (m)
$Q$	cathode capacity (Ah)
$q_n$	practical capacity of type $n$ particle ( $\text{Ah kg}^{-1}$ )
$R_{n,m}$	particle radius of active material $n$ with size class $m$ (m)
$R$	gas constant ( $8.314 \text{J mol}^{-1} \text{K}^{-1}$ )
$r$	radial distance within a particle of active material (m)
$T$	absolute temperature (K)
$t$	time(s)
$t_+^0$	lithium ion transference number
$U_{n,m}$	equilibrium potential for lithiation/delithiation on active material $n$ with particle size class $m$ (V)
$y_{n,m}$	lithium content in active material $n$ with particle size class $m$
Greek	
$\alpha_{n,m}$	solid state thermodynamic factor of active material $n$ with particle size class $m$
$\beta_n$	charge transfer coefficient for lithiation/delithiation on active material $n$
$\beta_f$	charge transfer coefficient for charge transfer reaction at lithium foil electrode
$\gamma$	Bruggeman exponent
$\xi$	total volume fraction of all cathode active material in the electrode
$\xi_{n,m}$	volume fraction of active material $n$ with particle size class $m$

$\xi'_{n,m}$	mass fraction of active material $n$ with particle size class $m$
$\varepsilon_{\text{cat}}$	porosity of cathode
$\varepsilon_{\text{sep}}$	porosity of separator
$\eta_{n,m}$	surface overpotential on active material $n$ with particle size class $m$ (V)
$\kappa$	electrolyte ionic conductivity ( $\text{S m}^{-1}$ )
$\kappa_{\text{eff,cat}}$	effective ionic conductivity in blended electrode ( $\text{S m}^{-1}$ )
$\rho_n$	density of type $n$ particle ( $\text{kg m}^{-3}$ )
$\sigma_{\text{eff}}$	effective electronic conductivity in blended electrode ( $\text{S m}^{-1}$ )
$\Phi_1$	solid-phase potential of cathode (V)
$\Phi_2$	liquid-phase potential of electrolyte (V)
$\Phi_f$	electrode potential of Li counter electrode (V)

## Subscript

$n$	active material type (NMC and LMO)
$m$	particle size class
cat	cathode
eff	effective
sep	separator
s	surface

measurements to analyze the lithiation and delithiation mechanisms of a gold film serving as a lithium-ion battery anode. Birkel et al. [18] used GITT to determine the equilibrium potentials of NMC and graphite electrodes, while Wu et al. [19] estimated the lithium ion solid-state diffusion coefficient in an NMC electrode based on a physicochemical model. However, GITT analysis of a blended electrode to investigate the thermodynamics and dynamic processes during charge-discharge has still not been reported. This method is particularly well suited to investigate the effects of the different size fractions and chemical composition and the interaction between the active components of a blended electrode, as will be shown in this work.

Both the optimization of electrode design and fundamental analysis of the behavior of battery electrodes benefit from physics-based mathematical models which can simulate the electrode response to an electrochemical process. Moreover, these models are able to compute certain quantities that are not easily measured. However, only few mathematical models of blended cathode systems have been reported. Albertus et al. [2] presented a model to describe the influence of NCA-LMO blended cathode composition on the charge-discharge curves based on a distribution of contact resistances between the active material and the conductive matrix. Jung [4] developed a model of an NMC-LMO cathode and graphite-soft carbon anode to simulate and predict their performance.

In our previous work [20], we developed a pseudo-two-dimensional (P2D) multi-particle model of an NMC-LMO blended cathode that was able to accurately describe the effect of the C-rate on the galvanostatic discharge and account for the effect of multiple particle sizes of the different active materials. In an earlier study [21], we showed that a simpler version of the model (i.e., no porous-electrode effects included) gave excellent fits to experimental potential-capacity and differential capacity curves at low rates and could be used to accurately predict the composition of a blended cathode. In the current work, the multi-particle model is adapted to describe the potential response of the same NMC-LMO cathode to intermittent galvanostatic pulses in order to gain further insight into the kinetic and thermodynamic parameters of the system. A particular focus of the GITT experiments in this study is to investigate the transport characteristics of intercalated

species between and within the active materials under the conditions of a small-current or short-time electrochemical perturbation. On the basis of the model, it is possible to resolve the separate charge-discharge characteristics of the NMC and LMO components in the blended cathode during the relaxation period after a short discharge pulse.

## 2. Experimental

In this work, coin cells were fabricated from a fresh and unused commercial pouch cell containing blended NMC-LMO cathode sheets coated on both sides of an aluminum current collector. Only one of these cathode sheets was used to make the coin cells. The solvent N-methyl-2-pyrrolidone (NMP) was applied to the cathode sheet on one of the sides to dissolve away the binder and allow the remaining cathode material to be easily wiped away and discarded. Electrode discs with  $0.712 \text{ cm}^2$  area were punched out of the NMC-LMO material remaining on the other side and then washed in dimethyl carbonate (DMC) to remove any salt deposited on their surface. Then, cathode|separator|Li coin cells were fabricated with a lithium foil as reference/counter electrode and Celgard 2500 as separator soaked in an electrolyte of 1 M  $\text{LiPF}_6$  dissolved in a 1:1 (weight basis) EC/DMC solution. The entire process above was conducted in an argon-filled glove box.

These coin cells were subjected to a series of tests using a battery cycler (Neware CT-3008-5V10 mA-164-U) at the room temperature. In order to ensure that each cell had attained the same stable state at the start of the GITT experiment, it was subjected to 5 consecutive CCCC formation cycles between a lower cut-off potential of 3 V and an upper potential of 4.2 V. The specific experimental waveform of the cycling was described in our previous study [20]. Following these 5 formation cycles, we subjected the coin cell to a GITT experiment. Each GITT experiment consisted of a sequence of 10 galvanostatic pulses at a given discharge current separated by a fixed relaxation period in which no current was applied. These pulses involved a discharge current of either 1C, C/2 or C/5 (corresponding to pulse widths of 6, 12 and 30 min, respectively) and an interval relaxation time of either 15 min or 2 h (1C rate corresponds to 1.38 mA of applied current). At each discharge current, GITT experiments were conducted at the two relaxation times in succession. A fresh coin cell was used for each of the three applied currents. This entire procedure was repeated a second time with a new set of fresh cells and found to yield very reproducible experimental data. Through a combination of each of these discharge currents and relaxation periods, six different GITT experiments were conducted. For example, the first GITT consisted of the following steps: i) charge at C/50 until a potential of 4.2 V was reached, ii) 2 h rest period, iii) discharge at 1C for 6 min, iv) 15 min rest period, v) repetition of steps iii) and iv) 9

times, vi) discharge at C/50 until a potential of 3.0 V was reached and vii) 2 h rest period. The purpose of steps i) and vi) was to ensure the cell was fully lithiated at the start of the GITT experiment and fully delithiated at the end of each experiment. The applied current and duration time in step iii) and rest period in step iv) were changed for each GITT experiment, as discussed above.

## 3. Mathematical model

To simulate the potential response of the NMC-LMO blended electrode to the intermittent galvanostatic pulses in the GITT experiments, the multi-particle mathematical model presented previously is implemented to describe the lithiation/delithiation dynamics at the particle and electrode scales [22,23]. The defining feature of the multi-particle model lies in considering each of the two active electrode components NMC and LMO to have a non-uniform particle size distribution consistent with the actual physical and material characteristics (Fig. 1). The model was verified in a previous study by successfully fitting it to experimental galvanostatic discharge curves [20]. The governing equations and corresponding boundary conditions at both the particle and electrode levels are shown in Table 1. The numerical values of the model parameters used are listed in Table 2. All equations and parameters were taken from Ref. [20] without any change. The system of equations was solved using the COMSOL Multiphysics 4.4 finite element software package.

## 4. Results and Discussion

### 4.1. Comparison of model simulations to experimental discharge GITT responses

As shown by the experimental and simulated responses in Fig. 2, the multi-particle model gives excellent predictions of the GITT curves in an NMC-LMO blended cathode over a wide range of discharge rates (1C, C/2 and C/5), pulse durations (6 min, 12 min and 30 min) and interval relaxation periods (15 min and 2 h). At the higher C-rates of 1C and C/2 and a relaxation period of 15 min (Fig. 2a and c), the simulated potential evolution during each of the middle four or five discharge pulses is slightly steeper than that actually measured. However, in the case of the smaller current of C/5 (Fig. 2e), the simulated potential remains very close to the experimental value over the majority of the GITT experiment. Moreover, the potential drop which becomes progressively smaller with each successive pulse is accurately tracked by the model. A comparison of the responses in Fig. 2a, c, e to Fig. 2b, d, f enables the effect of the length of the relaxation period (15 min to 2 hours) following each current pulse to be discerned for both the simulated and experimental responses. This analysis shows that the model

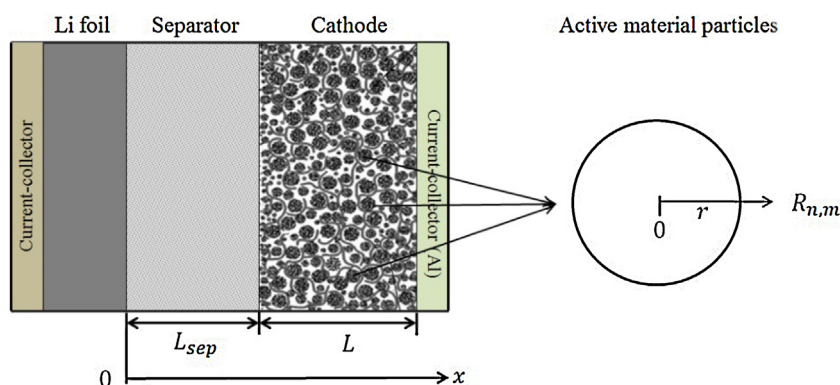


Fig. 1. Schematic diagram showing the cell configuration used for the pseudo-two-dimensional multi-particle model of the NMC-LMO blended cathode.

**Table 1**  
Summary of governing equations and corresponding boundary conditions [20].

<p>Particle-level equations</p> <p>Solid phase mass balance</p> $\frac{\partial c_{n,m}}{\partial t} = \frac{1}{r^2} \frac{\partial}{\partial r} \left( D_{n,m} r^2 \frac{\partial c_{n,m}}{\partial r} \right)$ $D_{n,m} = \alpha_{n,m} \mathcal{D}_n$ $\alpha_{n,m} = -\frac{F}{RT} y_{n,m} (1 - y_{n,m}) \frac{\partial U_{n,m}}{\partial y_{n,m}}$ $i_{n,m} = i_{n,m}^0 \left[ \exp\left(\frac{(1-\beta_n)F}{RT} \eta_{n,m}\right) - \exp\left(-\frac{\beta_n F}{RT} \eta_{n,m}\right) \right]$ $i_{n,m}^0 = F k_n (c_e)^{(1-\beta_n)} (c_{s,n,m})^{\beta_n} (c_n^{\max} - c_{s,n,m})^{\beta_n}$ $\eta_{n,m} = \Phi_1 - \Phi_2 - U_{n,m}(y_{n,m})$ $y_{n,m} = \frac{c_{n,m}}{c_n^{\max}}$ <p>Electrode-level equations</p> <p>Solid phase charge balance</p> $\mathbf{i}_1 = -\sigma_{\text{eff}} \nabla \Phi_1$ $\nabla \cdot \mathbf{i}_1 = -\xi \sum_{n=1}^N \sum_{m=1}^M \xi_{n,m} a_{n,m} i_{n,m}$ $\sum_{n=1}^N \sum_{m=1}^M \xi_{n,m} = 1$ $\xi_{n,m} = \frac{\xi'_{n,m} / \rho_n}{\sum_{n=1}^N \left( \sum_{m=1}^M \xi'_{n,m} / \rho_n \right)}$ $a_{n,m} = \frac{3}{R_{n,m}}$ $E = \Phi_1  _{x=L_{\text{sep}}+L} - \Phi_f$ <p>Liquid phase charge balance</p> $\nabla \cdot \mathbf{i}_2 = 0$ $\mathbf{i}_2 = -\kappa_{\text{eff,sep}} \nabla \Phi_2 + \frac{2\kappa_{\text{eff,sep}} RT (1-t_+^0)}{F c_e} \left( 1 + \frac{d \ln f_{\pm}}{d \ln c_e} \right) \nabla c_e$ $\kappa_{\text{eff,sep}} = \kappa_e^{\gamma_{\text{sep}}}$ $\nabla \cdot (\mathbf{i}_1 + \mathbf{i}_2) = 0$ $\mathbf{i}_2 = -\kappa_{\text{eff,cat}} \nabla \Phi_2 + \frac{2\kappa_{\text{eff,cat}} RT (1-t_+^0)}{F c_e} \left( 1 + \frac{d \ln f_{\pm}}{d \ln c_e} \right) \nabla c_e$ $\kappa_{\text{eff,cat}} = \kappa_e^{\gamma_{\text{cat}}}$ <p>Electrolyte mass balance</p> $e_{\text{sep}} \frac{\partial c_e}{\partial t} = \nabla \cdot (e_{\text{sep}} D_{\text{eff,sep}} \nabla c_e) - \frac{\mathbf{i}_2 \nabla t_+^0}{F}$ $D_{\text{eff,sep}} = D_e e_{\text{sep}}^{\gamma-1}$ $e_{\text{cat}} \frac{\partial c_e}{\partial t} = \nabla \cdot (e_{\text{cat}} D_{\text{eff,cat}} \nabla c_e) - \frac{\mathbf{i}_2 \nabla t_+^0}{F} + \frac{(1-t_+^0) \xi \sum_{n=1}^N \sum_{m=1}^M \xi_{n,m} a_{n,m} i_{n,m}}{F}$ $D_{\text{eff,cat}} = D_e e_{\text{cat}}^{\gamma-1}$ $D_e = \frac{c_e}{c_0} \left( 1 + \frac{d \ln f_{\pm}}{d \ln c_e} \right) \mathcal{D}_e$ <p>Lithium counter electrode kinetics</p> $I = -A i_f^0 \left[ \exp\left(\frac{(1-\beta_f)F}{RT} (\Phi_f - \Phi_2)\right) - \exp\left(-\frac{\beta_f F}{RT} (\Phi_f - \Phi_2)\right) \right]$ <p>Equilibrium potential</p> $U_{\text{NMC}}(y_{\text{NMC}}) = 6.51176 - 8y_{\text{NMC}} + 7.1086y_{\text{NMC}}^2 - 1.55y_{\text{NMC}}^3 - 0.459y_{\text{NMC}}^6 - 5.00034 \times 10^3 \exp(135.089y_{\text{NMC}}^2 - 118.089)$ $U_{\text{LMO}}(y_{\text{LMO}}) = 0.225 - 0.392y_{\text{LMO}} + 2.2 \tanh[-1010(y_{\text{LMO}} - 0.994)] + 1.9 \tanh[-21.4(y_{\text{LMO}} - 1.04)]$ $+ 0.181 \text{sech}[23.4(y_{\text{LMO}} - 0.397)] - 0.175 \text{sech}[24.2(y_{\text{LMO}} - 0.399)]$ $+ 0.0164 \text{sech}[13.1(y_{\text{LMO}} - 0.567)] + 0.33 \text{sech}[48.1(y_{\text{LMO}} - 1)]$	<p>Boundary conditions</p> $\frac{\partial c_{n,m}}{\partial r} = 0 \text{ at } r = 0$ $\frac{\partial c_{n,m}}{\partial r} = -\frac{i_{n,m}}{F D_{n,m}} \text{ at } r = R_{n,m}$ <p>Boundary conditions</p> $\mathbf{i}_1 = 0 \text{ at } x = L_{\text{sep}}$ $\mathbf{i}_1 = I/A \text{ at } x = L_{\text{sep}} + L$ <p>Boundary conditions</p> $\Phi_2 = 0 \text{ at } x = 0$ $\mathbf{i}_2  _{\text{sep}} = \mathbf{i}_2  _{\text{cat}} \text{ at } x = L_{\text{sep}}$ $\mathbf{i}_2  _{\text{sep}} = \mathbf{i}_2  _{\text{cat}} \text{ at } x = L_{\text{sep}}$ $\mathbf{i}_2 = 0 \text{ at } x = L_{\text{sep}} + L$ <p>Boundary conditions</p> $e_{\text{sep}} \frac{\partial c_e}{\partial x} = -\frac{I(1-t_+^0)}{F D_{\text{eff,sep}} A} \text{ at } x = 0$ $\frac{\partial c_e}{\partial x}  _{\text{sep}} = \frac{\partial c_e}{\partial x}  _{\text{cat}} \text{ at } x = L_{\text{sep}}$ $\frac{\partial c_e}{\partial x}  _{\text{sep}} = \frac{\partial c_e}{\partial x}  _{\text{cat}} \text{ at } x = L_{\text{sep}}$ $\frac{\partial c_e}{\partial x} = 0 \text{ at } x = L_{\text{sep}} + L$
--	--

becomes more accurate when the relaxation time after the discharge pulse is extended from 15 min to 2 h. This suggests that the model is more effective for those experiments with a long enough relaxation period for the system to return more closely to its equilibrium state.

It should be acknowledged that the model does not capture the observed behavior as well during the last two or three pulses in each of the experiments. When the cell is almost fully discharged, its measured potential tends to drop very rapidly, making it difficult for the simulations to closely track it. Also, in several cases, the simulation terminated early since the potential reached the lower cut-off value of 3.0 V (Fig. 2a, 2b and 2c). On the basis of the cases shown in Fig. 2, the model is most accurate for GITT discharge at lower rates (i.e., C/5, 30 min discharge time) with longer relaxation periods (i.e., 2 h) (Fig. 2f). Consequently, we restrict ourselves to these conditions in the subsequent analysis of the model to explore other aspects of the dynamics of the blended electrode during intermittent operation.

## 4.2. Current contribution analysis

The multi-particle model permits the contributions of the two active materials (LMO and NMC) to the internal dynamics of the blended cathode to be determined over the ten C/5 discharge pulses of the GITT experiment shown in Fig. 3, each of which is followed by 2 h relaxation. The LMO component contributes a higher proportion of the overall current than NMC during the first three pulses. Also, the LMO contribution over the first five pulses or the first half of the GITT process (Fig. 3a) is similar to that obtained in our previous galvanostatic discharge experiment [20]. When the operation of the cell is shifted into the relaxation phase after the discharge pulses, the currents due to both NMC and LMO do not immediately decrease to zero. In fact, the currents have not yet reached zero by the end of each of the 2 h relaxation periods that follow the first five pulses (Fig. 3b). Obviously, the current generated by LMO is always opposite in sign and exactly cancelled by the current generated by NMC during the relaxation periods. In

**Table 2**  
List of model parameters [20].

Parameter	Symbol	LMO	NMC
Cathode area (cm <sup>2</sup> )	<i>A</i>		0.712 <sup>m</sup>
Electrode thickness (m)	<i>L</i>		5.7 × 10 <sup>-5</sup> m
Cathode capacity (Ah)	<i>Q</i>		0.002 <sup>m</sup>
Total active-material volume fraction	$\xi$		0.558 [21]
Radius of type <i>n</i> particle in size class <i>m</i> (m)	<i>R<sub>n,m</sub></i>	8.7 × 10 <sup>-7</sup> m	4.65 × 10 <sup>-6</sup> m (micron group) 4.35 × 10 <sup>-7</sup> m (submicron group)
Mass fraction of type <i>n</i> particle among total active materials	$\xi'_{n,m}$	0.3 [21]	0.22 [20] (micron group) 0.48 [20] (submicron group)
Rate constant for charge transfer on type <i>n</i> cathode particle (mol/[m <sup>2</sup> s(mol m <sup>-3</sup> ) <sup>1.5</sup> ])	<i>k<sub>n</sub></i>	3 × 10 <sup>-11</sup> [20]	3 × 10 <sup>-11</sup> [20]
Binary diffusion coefficient of Li in type <i>n</i> particle (m <sup>2</sup> s <sup>-1</sup> )	<i>D<sub>n</sub></i>	1.0 × 10 <sup>-16</sup> [20]	1.1 × 10 <sup>-16</sup> [20]
Capacity of type <i>n</i> particle (Ah kg <sup>-1</sup> )	<i>q<sub>n</sub></i>	100 [2]	151 [19]
Maximum lithium concentration in type <i>n</i> particle (mol m <sup>-3</sup> )	<i>c<sub>n</sub><sup>max</sup></i>	23339 [2]	49761 [19]
Density of type <i>n</i> particle (kg m <sup>-3</sup> )	$\rho_n$	4220 [21]	4770 [21]
Charge-transfer coefficient for charge transfer on type <i>n</i> cathode particle	$\beta_n$	0.5 [20]	0.5 [20]
Electrode porosity	$\varepsilon_{cat}$		0.35 [20]
Initial electrolyte concentration (mol m <sup>-3</sup> )	<i>c<sub>e</sub></i>		1000 <sup>m</sup>
Separator thickness (m)	<i>L<sub>sep</sub></i>		2.5 × 10 <sup>-5</sup> Celgard
Lithium ions transference number	<i>t<sub>+</sub><sup>0</sup></i>		0.36 [20]
Bulk diffusion coefficient in the electrolyte (m <sup>2</sup> s <sup>-1</sup> )	<i>D<sub>e</sub></i>		5.2 × 10 <sup>-10</sup> [24]
Bulk ionic conductivity of the electrolyte (S m <sup>-1</sup> )	$\kappa$		1.3 [24]
Charge-transfer coefficient for charge transfer on Li foil electrode	$\beta_f$		0.5 [20]
Separator porosity	$\varepsilon_{sep}$		0.55 <sup>Celgard</sup>
Bruggeman exponent	$\gamma$		1.5 [20]
Effective electronic conductivity (S m <sup>-1</sup> )	$\sigma_{eff}$		10.10 <sup>m</sup>
Exchange current density on Li foil electrode (A m <sup>-2</sup> )	<i>i<sub>f</sub><sup>0</sup></i>		20 [20]
Faraday constant (C mol <sup>-1</sup> )	<i>F</i>		96478
Gas constant (J mol <sup>-1</sup> K <sup>-1</sup> )	<i>R</i>		8.314
Temperature (K)	<i>T</i>		298

m: measured.

Celgard: Celgard product data sheet.

order to examine the dynamics of this process in more detail, the responses of two current pulses marked PULSE 1 and PULSE 2 in Fig. 3a (magnified in Fig. 4) are examined. PULSE 1 shows the response during the 1st pulse applied during the GITT experiment, whereas PULSE 2 corresponds to the 5th pulse in the sequence of ten. Throughout the 30 min of discharge during PULSE 1, more current flows through LMO than through NMC (Fig. 4a). Once the current is turned off at the start of the relaxation period, the NMC current changes instantaneously in the negative direction and then becomes positive again relatively soon afterward (Fig. 4a, 4b). LMO continues to be discharged (i.e., positive current), albeit at a decreasing rate, over the time period marked by points A and B, while NMC is now being charged (i.e., negative current). This signifies that lithium is being transferred from NMC to LMO within the cathode over this relatively short time period. The preferential discharge of LMO over that of NMC is consistent with the finding above that most of the discharge current during the first few pulses flows through LMO. This trend continues until point B is reached, whereupon the LMO and NMC currents both pass through zero and a crossover occurs. At this crossover point, the electrode is not stabilized although the current flowing through component is zero. Thereafter, NMC is discharged and LMO is charged over the remainder of the relaxation period. Over this last portion of the relaxation period, the magnitudes of both currents first rise to a maximum and then gradually decrease back toward zero.

Since PULSE 2 occurs midway through the GITT, LMO has reached close to a fully lithiated state, whereas NMC has not (Fig. 8 in Ref. [20]) when this pulse begins. Not surprisingly, the LMO current is much lower than the NMC current during the 30 min discharge period of PULSE 2, as shown in Fig. 4c. The subsequent

charge-discharge behavior during the segments DE and EF of the relaxation period (Fig. 4d) follows the same trend as that during the segments AB and BC, respectively, that follow PULSE 1 (Fig. 4b), i.e., first discharge and then charge of LMO and the opposite for NMC. The main difference between the electrode dynamics during the relaxation periods of PULSE 1 and PULSE 2 is the change of current and the relative length of time in which LMO and NMC are discharged and charged, which is associated with the degree of lithiation of LMO and NMC. Since LMO is much more fully lithiated by the time PULSE 2 starts, the change in discharge current is relatively small and the first charge-discharge period DE takes more time than the corresponding segment AB in PULSE 1.

As found in our previous study [20], the particle sizes of the NMC component in this commercial blended cathode can best be described in terms of two separate particle size distributions (PSDs) – a submicron group with *d*<sub>50</sub> of 0.87 μm and a micron group with *d*<sub>50</sub> of 9.29 μm. Therefore, the overall current due to NMC can be broken down into contributions from these two size groups. Fig. 5 presents the breakdown of the current contributed from these two groups over the course of the same GITT experiment shown in Figs. 3 and 4.

Fig. 5a shows that the current due to the NMC submicron particles far exceeds that of the NMC micron particles throughout all 30 min of each discharge pulse during the GITT experiment. During each of the following 2 h relaxation periods, the submicron particles are always charging while the micron particles are discharging, albeit at ever diminishing rates with each pulse. This behaviour is clearly evident during PULSE 1 and 2 (Fig. 5b and c). In the absence of an external current, the losses associated with reaction kinetics at the surface and species transport within the

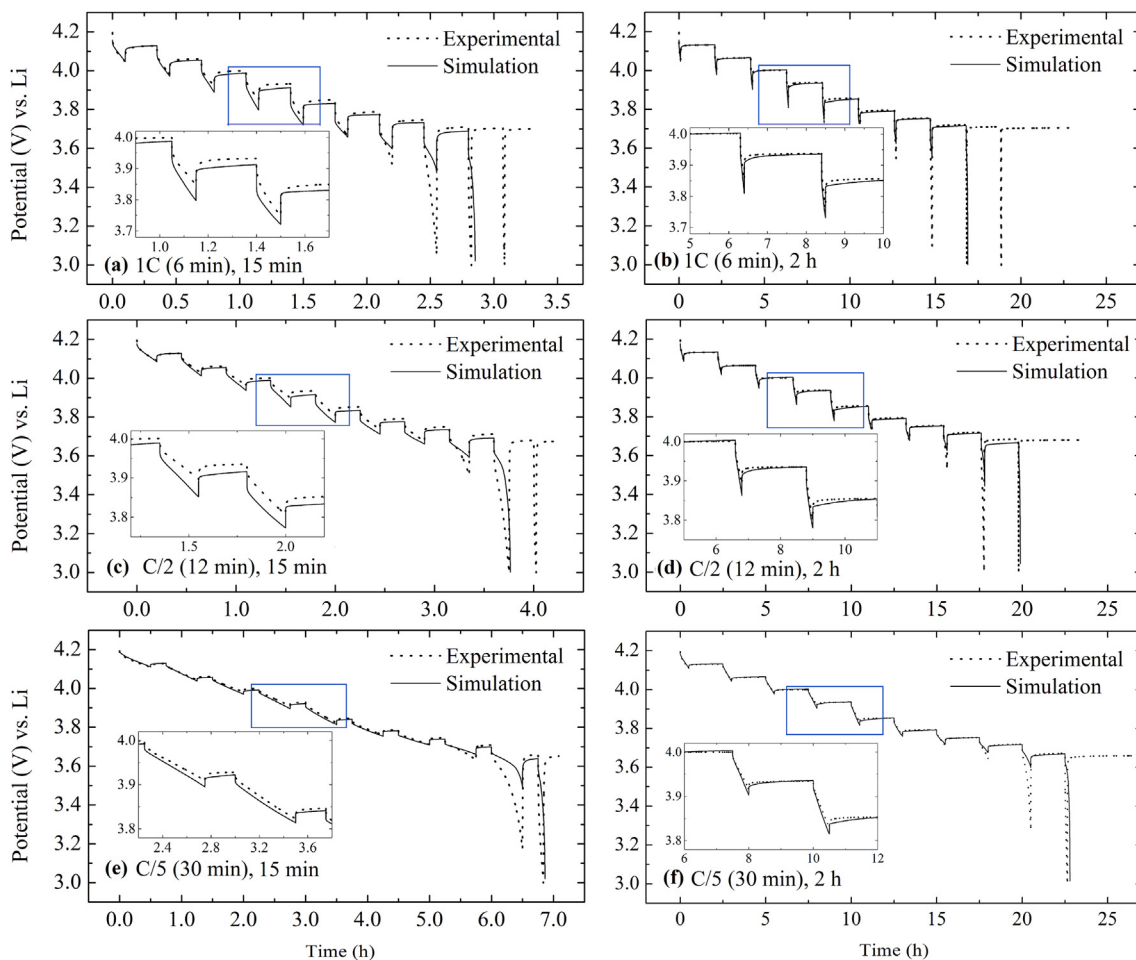


**Fig. 2.** Comparison of the experimental and simulated responses to the GITT pulses consisting of the following discharge currents and rest intervals: (a) 1C (6 min), 15 min (b) 1C (6 min), 2 h (c) C/2 (12 min), 15 min (d) C/2 (12 min), 2 h (e) C/5 (30 min), 15 min rest (f) C/5 (30 min), 2 h.

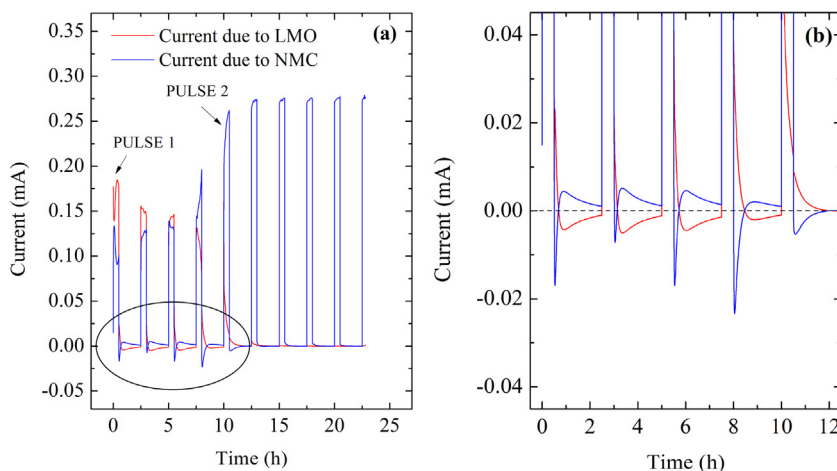


**Fig. 3.** (a) Variation of the LMO and NMC currents with time over the course of the ten GITT discharge pulses conducted at C/5 (30 min) followed by 2 h relaxation. The circled region in (a) is shown at higher resolution in (b).

active particles diminish. The electrode dynamics which is controlled by an external current during the on-time is now determined by the deviation of the active particle equilibrium potentials  $U_{n,m}(y_{s, nm})$  from a “common potential” throughout the electrode during the relaxation period. The smaller “over-lithiated” NMC submicron particles with a lower surface equilibrium

potential give away a fraction of their content to the larger “under-lithiated” micron-sized NMC particles with a higher equilibrium potential to compensate the lithiation lag during the on-time. Since the two particles have the same chemical nature, they must have identical Li concentrations at their surfaces in order to reach a common equilibrium potential. On the other hand, the

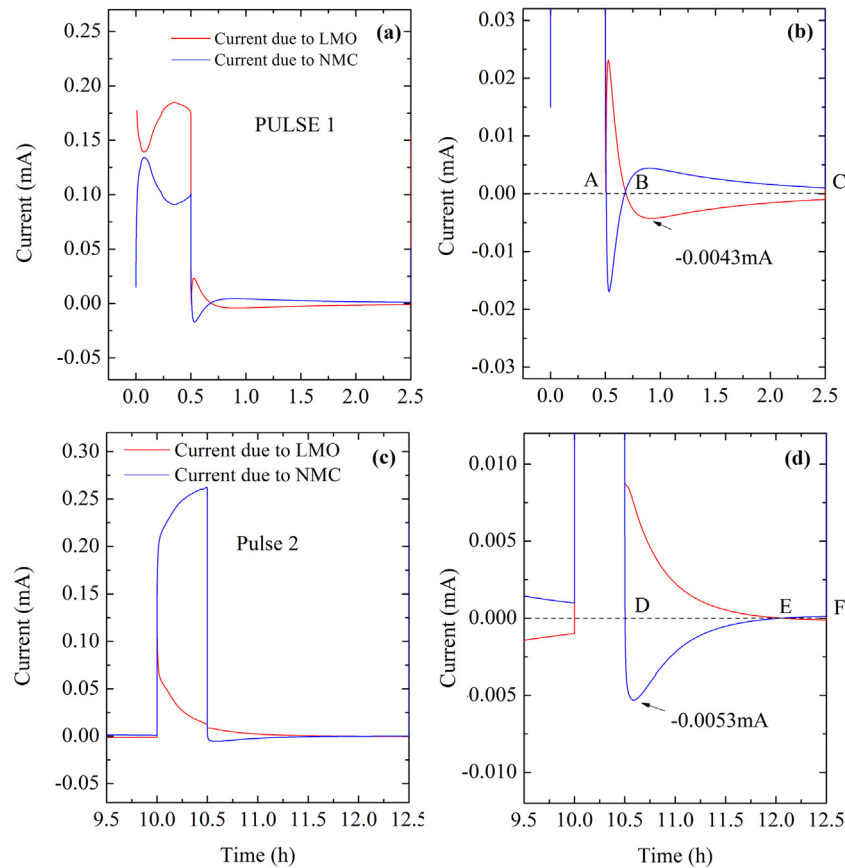


**Fig. 4.** (a) Variation of the LMO and NMC currents with time for (a) PULSE 1 and (c) PULSE 2. The circled regions in (a) and (c) are shown at higher resolution in (b) and (d), respectively.

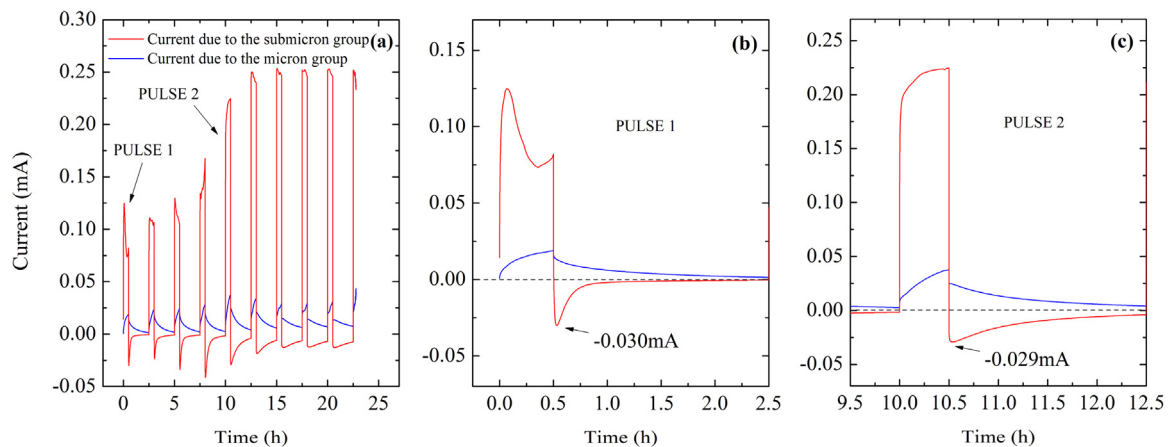


**Fig. 5.** (a) Current contributions of the NMC submicron and micron groups over the course of the same GITT experiment presented in Figs. 3 and 4. Magnified views of current contributions during PULSE 1 and PULSE 2 are shown in (b) and (c), respectively.

concentration gradient within each particle is expected to disappear during the relaxation period depending on its initial value, particle size and solid-state chemical diffusion coefficient. As a result, the relaxation dynamics at the particle level involves two distinct mechanisms simultaneously: i) intra-particle relaxation of the concentration gradient toward a flatter profile over time and ii) inter-particle exchange of lithium to reach a common equilibrium potential at the surfaces of the two types of NMC particles. Given enough relaxation time, the final concentration of Li is expected to be identical in the submicron- and micron-sized NMC particles. Similar effects should operate between NMC and

LMO particles except for the fact that the lithium contents of the two types of active materials are not identical at equilibrium state but determined in accordance with the individual equilibrium potential curve of each material.

#### 4.3. Surface lithium stoichiometry analysis

The variation of lithium stoichiometry at the surface of each particle group over the ten pulses in the blended cathode simulated by the model is presented in Fig. 6a. The responses during PULSE 1 and PULSE 2 are shown at a higher resolution in

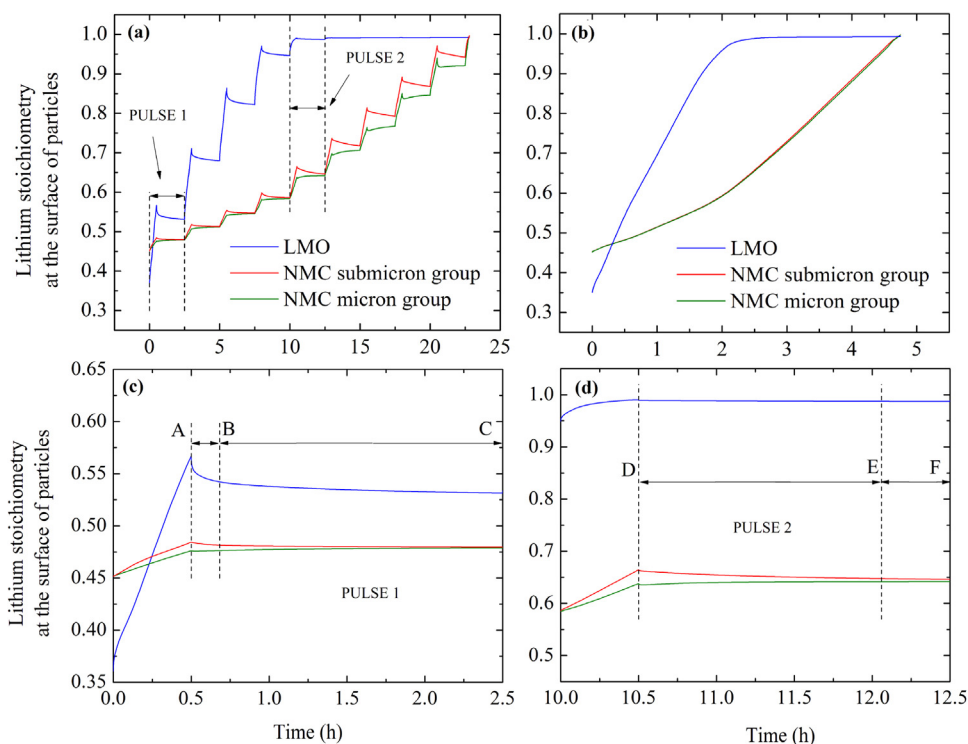


**Fig. 6.** Simulated variation of the lithium stoichiometry at the surfaces of particles (a) over the course of the GITT experiment and (b) during galvanostatic discharge at the rate of  $C/5$  in the NMC-LMO blended cathode. PULSES 1 and 2 in (a) are shown at higher resolution in (c) and (d), respectively, including the segments defined in Fig. 4b and d.

Fig. 6c and d, respectively, including the same segments AB, BC, DE and EF defined in Fig. 4b and d. The maximum lithium concentration is always reached on the surfaces of both LMO and NMC submicron particles by the end of each discharge pulse. However, over the subsequent relaxation period, the surface concentration decreases gradually until the beginning of the next discharge pulse. The relaxation of the surface concentration is smaller (less than 10% for LMO and 5% for NMC comparing concentrations at the beginning and end of relaxation), indicating the relatively weak driving forces in effect for both inter- and intra-particle relaxation. On the other hand, the lithium concentration remains almost constant at the surface of the NMC micron particles during the first few relaxation periods, but then eventually begins to rise during the later relaxation periods. In addition, the lithium stoichiometry at the surface of the LMO particles reaches close to 1.0 after 5 or 6 discharge pulses which is close to the midpoint of the entire GITT experiment. Interestingly, the lithium stoichiometry at the surface also reaches close to 1.0 midway through the continuous galvanostatic discharge of the blended cathode at the same rate of  $C/5$  (Fig. 6b). The electrode dynamics in the first half of the GITT and continuous discharge experiments is mostly dominated by LMO lithiation. As a result, LMO becomes fully lithiated prior to and faster than NMC due to thermodynamic reasons (i.e., a higher equilibrium potential of LMO compared to NMC, as seen in Fig. 3 of Ref [21]). During the second half of the GITT experiment, however, NMC submicron and micron particles carry most of the Li flux during the current pulse and exchange matter mostly with each other (i.e., little interaction with LMO) during relaxation (Fig. 6a and d). Unlike the first half of the GITT experiment, NMC particles do not completely reach an equilibrium state (i.e., identical surface concentration) in the second half of the experiment although the deviation from a final equilibrium state is very small (i.e., only less than 3%). Overall, analysis of the surface concentrations confirms that the lithium lost from the surfaces of the LMO and NMC submicron particles either diffuses into the

interior of these particles or to the NMC micron particles, which is consistent with the results shown in Fig. 5.

Fig. 7 shows a comparison between continuous and intermittent galvanostatic discharge data both at  $C/5$ . No significant difference in the end-capacity of the electrode is observed between the two operating conditions. In other words, solid-state diffusion is relatively fast (more specifically, diffusion of Li in NMC particles) and the relaxation steps in the GITT experiment, which permit redistribution of matter within each and among all of the active particles, have little or no impact on diffusion barriers towards the end of discharge. This is in line with the surface concentrations shown in Fig. 6a and 6b all having reached close to unity at the end of discharge under both operating conditions. It should be noted that NMC particles mainly determine the end of the discharge process since LMO particles are already fully lithiated midway through discharge.

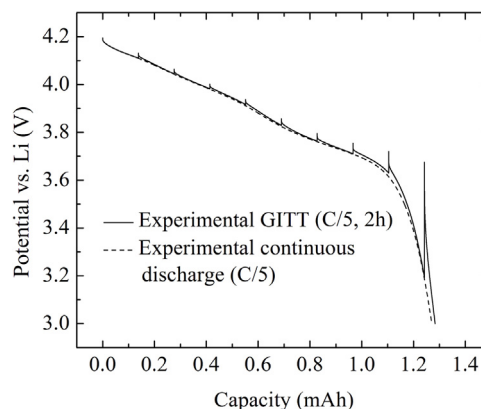


**Fig. 7.** Comparison of the experimental GITT ( $C/5$ , 2h) and continuous discharge data at the same rate of  $C/5$ .

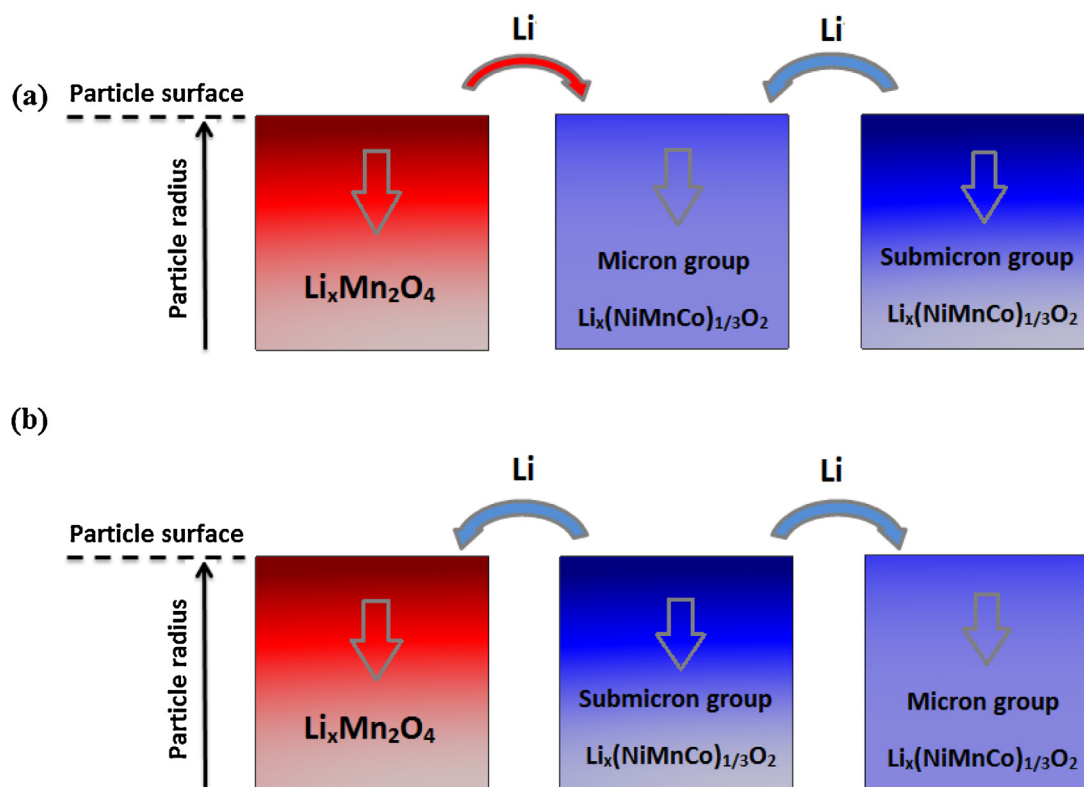


**Fig. 8.** Schematic diagram showing the flow of lithium between particles during the BC and EF in Figs. 4 b and 6 c, and AB and DE in Figs. 4 d and 6 d, of the relaxation period of GITT experiment, corresponding with: (a) from LMO and NMC submicron particles to NMC micron particles and (b) from NMC submicron particles to LMO and NMC micron particles, separately.

A schematic diagram describing the flow of lithium between the LMO and NMC submicron and micron particles during the relaxation period can be developed by combining the results from these simulations (Fig. 8). Fig. 8a shows the lithium flows into the NMC micron particles from LMO and NMC submicron particles as the former are discharging and the latter are charging. This is consistent with the variation of surface lithium concentration during each of the relaxation periods in Fig. 6a, the current contributions of the blended cathode components in Fig. 5 and the behavior observed during periods BC in Fig. 4a and EF in Fig. 4b. Based on the currents during periods AB in Fig. 4a and DE in Fig. 4b, another mode of internal charge-discharge dynamics is observed during the initial portions of the relaxation period of the first few GITT pulses and is shown in Fig. 8b, i.e., lithium flows into LMO and NMC micron particles from NMC submicron particles. However, despite this change in mode of internal electrode dynamics during the relaxation period, the surface lithium stoichiometry on the LMO and NMC micron particles decreases monotonically throughout this period (Fig. 6). This is possible due to the rapid internal diffusion of lithium within the particles which prevents any build-up on their surfaces.

The multi-particle model reveals that the different active materials and size groups in the NMC-LMO blended cathode interact strongly during operation. More specifically, lithium can flow between the LMO and NMC particles, which may influence their surface stoichiometries when the test cell is at open-circuit. Equilibrium may not be attained in time due to the differences in lithiation/delithiation kinetics of the two components. Another factor may be the different diffusion rates within the different sized NMC particles. However, no direct experimental evidence currently confirming this internal charge-discharge phenomenon predicted by the model has been reported in the literature, to the best of our knowledge.

As previously shown, Mn dissolution from LMO is the primary reason for its capacity loss and the formation of a secondary Li-rich, low-capacity phase at the surface of LMO particles [11,25–27]. Furthermore, the synergistic interplay between LMO and NMC has been experimentally confirmed [11–13], i.e., the presence of NMC lowers the LMO fade rate in NMC-LMO blended cathodes compared with that of single-component LMO electrodes.

The simulations indicate that the interaction between the electrode components has a balancing effect on the lithium concentration at the surfaces of LMO and NMC particles and tends to prevent the accumulation of excess lithium on the surface of LMO particles. This has the important effect of lowering the likelihood of the irreversible generation of a secondary Li-rich phase that could be the cause of LMO fade. These results can also form the basis of a future experimental study of the mechanistic interplay between LMO and NMC in these blended cathodes.

## 5. Conclusions

In this work, the multi-particle mathematical model presented previously [20] has been applied to simulate six sets of discharge GITT curves with varying pulse currents and relaxation periods obtained from an NMC-LMO blended lithium-ion electrode. The simulation results show that the model is applicable for all cases and more accurate for the case of small current pulse discharge rate with a longer relaxation time. An analysis of the current contribution and surface lithium stoichiometry of each component reveals that a complex interaction between the two active materials NMC and LMO and between micron and submicron NMC particles occurs during electrode operation. It has a balancing effect on the lithium concentration at the surfaces of LMO and NMC particles. The present analysis suggests that such interaction arises mainly from thermodynamic factors where the potentials of the

two components are driven away from (or toward) a common equilibrium potential during the on-time (or off-time).

### Acknowledgment

The authors gratefully acknowledge the funding provided by the General Motors Co., Automotive Partnership Canada (Project APCPJ 395996-09) and the Natural Sciences and Engineering Research Council of Canada (Project RGPIN-170912).

### References

- [1] S.B. Chikkannanavar, D.M. Bernardi, L. Liu, A review of blended cathode materials for use in Li-ion batteries, *J. Power Sources* 248 (2014) 91–100.
- [2] P. Albertus, J. Christensen, J. Newman, Experiments on and modeling of positive electrodes with multiple active materials for lithium-ion batteries, *J. Electrochem. Soc.* 156 (2009) A606–A618.
- [3] Y.L. Dai, L. Cai, R.E. White, Simulation and analysis of stress in a Li-ion battery with a blended  $\text{LiMn}_2\text{O}_4$  and  $\text{LiNi}_{0.8}\text{Co}_{0.15}\text{Al}_{0.05}\text{O}_2$  cathode, *J. Power Sources* 247 (2014) 365–376.
- [4] S. Jung, Mathematical model of lithium-ion batteries with blended-electrode system, *J. Power Sources* 264 (2014) 184–194.
- [5] J.P. Schmidt, H.Y. Tran, J. Richter, E. Ivers-Tiffée, M. Wohlfahrt-Mehrens, Analysis and prediction of the open circuit potential of lithium-ion cells, *J. Power Sources* 239 (2013) 696–704.
- [6] H.S. Kim, M. Kong, K. Kim, I.J. Kim, H.B. Gu, Electrochemical characteristics of  $\text{LiFePO}_4/\text{LiCoO}_2$  mixed electrode for Li secondary battery, *J. Electroceramics* 23 (2009) 219–224.
- [7] C. Qiu, L. Liu, F. Du, X. Yang, C. Wang, G. Chen, Y. Wei, Electrochemical performance of  $\text{LiMn}_2\text{O}_4/\text{LiFePO}_4$  blend cathodes for lithium ion batteries, *Chem. Res. Chinese Univ* 31 (2015) 270–275.
- [8] D.H. Jang, Y.J. Shin, S.M. Oh, Dissolution of spinel oxides and capacity losses in 4 V  $\text{Li}/\text{Li}_x\text{Mn}_2\text{O}_4$  Cells, *J. Electrochem. Soc.* 143 (1996) 2204–2211.
- [9] J. Vetter, P. Novák, M.R. Wagner, C. Veit, K.C. Möller, J.O. Besenhard, M. Winter, M. Wohlfahrt-Mehrens, C. Vogler, A. Hammouche, Ageing mechanisms in lithium-ion batteries, *J. Power Sources* 147 (2005) 269–281.
- [10] K. Amine, J. Liu, S. Kang, I. Belharouak, Y. Hyung, D. Vissers, G. Henriksen, Improved lithium manganese oxide spinel/graphite Li-ion cells for high-power applications, *J. Power Sources* 129 (2004) 14–19.
- [11] A.J. Smith, S.R. Smith, T. Byrne, J.C. Burns, J.R. Dahn, Synergies in blended  $\text{LiMn}_2\text{O}_4$  and Li  $[\text{Ni}_{1/3}\text{Mn}_{1/3}\text{Co}_{1/3}]\text{O}_2$  positive electrodes, *J. Electrochem. Soc.* 159 (2012) A1696–A1701.
- [12] H. Kitao, T. Fujihara, K. Takeda, N. Nakanishi, T. Nohma, High-temperature storage performance of Li-ion batteries using a mixture of Li–Mn spinel and Li–Ni–Co–Mn oxide as a positive electrode material, *Electrochem. Solid-State Lett.* 8 (2005) A87–A90.
- [13] S.K. Jeong, J.S. Shin, K.S. Nahm, T.P. Kumar, A.M. Stephan, Electrochemical studies on cathode blends of  $\text{LiMn}_2\text{O}_4$  and Li  $[\text{Li}_{1/15}\text{Ni}_{1/5}\text{Co}_{2/5}\text{Mn}_{1/3}\text{O}_2]$ , *Mater. Chem. Phys.* 111 (2008) 213–217.
- [14] D.W. Dees, D.P. Abraham, W. Lu, K.G. Gallagher, M. Bettge, A.N. Jansen, Electrochemical modeling and performance of a lithium-and manganese-rich layered transition-metal oxide positive electrode, *J. Electrochem. Soc.* 162 (2015) A559–A572.
- [15] S.R. Gowda, D.W. Dees, A.N. Jansen, K.G. Gallagher, Examining the electrochemical impedance at low states of charge in lithium-and manganese-rich layered transition-metal oxide electrodes, *J. Electrochem. Soc.* 162 (2015) A1374–A1381.
- [16] K.G. Gallagher, D.W. Dees, A.N. Jansen, D.P. Abraham, S.-H. Kang, A volume averaged approach to the numerical modeling of phase-transition intercalation electrodes presented for  $\text{Li}_x\text{C}_6$ , *J. Electrochem. Soc.* 159 (2012) A2029–A2037.
- [17] P. Bach, M. Stratmann, I. Valencia-Jaime, A.H. Romero, F.U. Renner, Lithiation and delithiation mechanisms of gold thin film model anodes for lithium ion batteries: electrochemical characterization, *Electrochim. Acta* 164 (2015) 81–89.
- [18] C.R. Birkl, E. McTurk, M.R. Roberts, P.G. Bruce, D.A. Howey, A parametric open circuit voltage model for lithium ion batteries, *J. Electrochem. Soc.* 162 (2015) A2271–A2280.
- [19] S.L. Wu, W. Zhang, X. Song, A.K. Shukla, G. Liu, V. Battaglia, V. Srinivasan, High rate capability of  $\text{Li}(\text{Ni}_{1/3}\text{Mn}_{1/3}\text{Co}_{1/3})\text{O}_2$  electrode for Li-ion batteries, *J. Electrochem. Soc.* 159 (2012) A438–A444.
- [20] Z. Mao, M. Farkhondeh, M. Pritzker, M. Fowler, Z. Chen, Multi-particle model for a commercial blended lithium-ion electrode, *J. Electrochem. Soc.* 163 (2016) A458–A469.
- [21] Z. Mao, M. Farkhondeh, M. Pritzker, M. Fowler, Z. Chen, M. Safari, Model-based prediction of composition of an unknown blended lithium-ion battery cathode, *J. Electrochem. Soc.* 162 (2015) A716–A721.
- [22] M. Doyle, T.F. Fuller, J. Newman, Modeling of galvanostatic charge and discharge of the lithium/polymer/insertion cell, *J. Electrochem. Soc.* 140 (1993) 1526–1533.
- [23] J. Newman, K.E. Thomas-Alyea, *Electrochemical Systems*, Wiley Hoboken, NJ, 2004.
- [24] M. Farkhondeh, M. Safari, M. Pritzker, M. Fowler, T. Han, J. Wang, C. Delacourt, Full-range simulation of a commercial  $\text{LiFePO}_4$  electrode accounting for bulk and surface effects: a comparative analysis, *J. Electrochem. Soc.* 161 (2014) A201–A212.
- [25] A. Du Pasquier, A. Blyr, P. Courjal, D. Larcher, G. Amatucci, B. G'erand, J.-M. Tarascon, Mechanism for limited 55 °C storage performance of  $\text{Li}_{1.05}\text{Mn}_{1.95}\text{O}_4$  electrodes, *J. Electrochem. Soc.* 146 (1999) 428–436.
- [26] J.M. Tarascon, A.S. Gozdz, C. Schmutz, F. Shokoohi, P.C. Warren, Performance of Bellcore's plastic rechargeable Li-ion batteries, *Solid State Ionics* 86 (1996) 49–54.
- [27] M.M. Thackeray, A. De Kock, M.H. Rossouw, D. Liles, R. Bittihn, D. Hoge, Spinel electrodes from the Li–Mn–O system for rechargeable lithium battery applications, *J. Electrochem. Soc.* 139 (1992) 363–366.